

The MUSE eXtremely Deep Field: Detections of circumgalactic Si II* emission at $z \gtrsim 2$ *

Haruka Kusakabe^{1,2**}, Valentin Mauerhofer³, Anne Verhamme², Thibault Garel², Jérémy Blaizot⁴, Lutz Wisotzki⁵, Johan Richard⁴, Leindert A. Boogaard⁶, Floriane Leclercq⁷, Yucheng Guo⁴, Adélaïde Claeysens⁸, Thierry Contini⁹, Edmund Christian Herenz¹⁰, Josephine Kerutt³, Michael V. Maseda¹¹, Leo Michel-Dansac^{4,12}, Themiya Nanayakkara¹³, Masami Ouchi^{1, 14, 15, 16}, Ismael Pessa⁵, and Joop Schaye¹⁷

¹ National Astronomical Observatory of Japan, 2-21-1 Osawa, Mitaka, Tokyo, 181-8588, Japan

² Observatoire de Genève, Université de Genève, 51 Chemin de Pégase, 1290 Versoix, Switzerland

³ Kapteyn Astronomical Institute, University of Groningen, P.O. Box 800, 9700 AV Groningen, The Netherlands

⁴ Univ. Lyon, Univ. Lyon1, Ens de Lyon, CNRS, Centre de Recherche Astrophysique de Lyon UMR5574, F-69230, Saint-Genis-Laval, France

⁵ Leibniz-Institut für Astrophysik Potsdam (AIP), An der Sternwarte 16 14482 Potsdam, Germany

⁶ Max Planck Institute for Astronomy, Königstuhl 17, 69117 Heidelberg, Germany

⁷ Department of Astronomy, The University of Texas at Austin, 2515 Speedway, Stop C1400, Austin, TX 78712-1205, USA

⁸ The Oskar Klein Centre, Department of Astronomy, Stockholm University, AlbaNova, SE-10691 Stockholm, Sweden

⁹ Institut de Recherche en Astrophysique et Plan, Toulouse 14, avenue E. Belin, 31400, France

¹⁰ Inter-University Centre for Astronomy and Astrophysics, Ganeshkind, Post Bag 4, Pune 41007, India

¹¹ Department of Astronomy, University of Wisconsin-Madison, 475 N. Charter St., Madison, WI 53706, USA

¹² Aix Marseille Univ, CNRS, CNES, LAM, Marseille, France

¹³ Centre for Astrophysics and Supercomputing, Swinburne University of Technology, Hawthorn, Victoria 3122, Australia

¹⁴ Institute for Cosmic Ray Research, The University of Tokyo, 5-1-5 Kashiwanoha, Kashiwa, Chiba 277-8582, Japan

¹⁵ Kavli Institute for the Physics and Mathematics of the Universe (WPI), University of Tokyo, Kashiwa, Chiba 277-8583, Japan

¹⁶ Department of Astronomical Science, SOKENDAI (The Graduate University for Advanced Studies), Osawa 2-21-1, Mitaka, Tokyo, 181-8588, Japan

¹⁷ Leiden Observatory, Leiden University, PO Box 9513, NL-2300 RA Leiden, The Netherlands

June 10, 2024

ABSTRACT

Context. The circumgalactic medium (CGM) serves as a baryon reservoir that connects galaxies to the intergalactic medium and fuels star formation. The spatial distribution of the metal-enriched cool CGM has not yet been directly revealed at cosmic noon ($z \approx 2-4$), as bright emission lines at these redshifts are not covered by optical integral field units.

Aims. To remedy this situation, we aim for the first-ever detections and exploration of extended Si II* emission (low-ionization state, LIS), referred to as “Si II* halos”, at redshifts ranging from $z = 2$ to 4 as a means to trace the metal-enriched cool CGM.

Methods. We use a sample of 39 galaxies with systemic redshifts of $z = 2.1-3.9$ measured with the [C III] doublet in the MUSE Hubble Ultra Deep Field catalog, which contains integration times spanning from ≈ 30 to 140 hours. We search for extended Si II* $\lambda 1265$, 1309, 1533 emission (fluorescent lines) around individual galaxies. We also stack a subsample of 14 UV-bright galaxies.

Results. We report five individual detections of Si II* $\lambda 1533$ halos. We also confirm the presence of Si II* $\lambda 1533$ halos in stacks for the subsample containing UV-bright sources. The other lines do not show secure detections of extended emission in either individual or stacking analyses. These detections may imply that the presence of metal-enriched CGM is a common characteristic for UV-bright galaxies. To investigate whether the origin of Si II* is continuum pumping as suggested in previous studies, we check the consistency of the equivalent width (EW) of Si II* emission and the EW of Si II absorption for the individual halo object with the most reliable detection. We confirm the equivalence, suggesting that photon conservation works for this object and pointing toward continuum pumping as the source of Si II*. We also investigate Si II* lines in a RAMSES-RT zoom-in simulation including continuum pumping and find ubiquitous presence of extended halos.

Key words. Galaxies: high-redshift – galaxies: formation – galaxies: evolution – galaxies: halos

1. Introduction

The circumgalactic medium (CGM) is the baryonic matter that envelops galaxies. The most common definition of the CGM is

the gas outside the interstellar medium (ISM) and inside the virial radius of the host dark matter halo. This region serves as a dynamic interface connecting galaxies to the intergalactic medium (IGM). Metals are ejected from galaxies to the CGM via outflows powered by supernovae explosions, stellar winds, and active galactic nuclei (AGNs). A part of those metals may be mixed with inflowing pristine and recycled gas and accrete onto the galaxies. Hence, the CGM is a gas and metal reservoir

* Based on observations made with ESO telescope at the La Silla Paranal Observatory under the large program 1101.A-0127

** e-mail: haruka.kusakabe.takeishi@gmail.com, haruka.kusakabe@nao.ac.jp

of a galaxy and plays a pivotal role in galaxy evolution (e.g., Tumlinson et al. 2017; Péroux & Howk 2020).

Historically, the CGM has been observed in absorption imprinted on quasi-stellar object (QSO) spectra (e.g., Wolfe et al. 1986). This method can trace a wide range of column densities and ionization states of various elements. The CGM is found to be a multiphase medium in terms of its density, temperature, ionization, kinematics, metallicity, and structure (e.g., Werk et al. 2016; Steidel et al. 2016; Chen et al. 2020; Schroetter et al. 2021). However, this method is limited to the lines of sight of background sources. Large programs with recent or upcoming instruments targeting bright galaxies as background sources (tomographic mapping) can reach the IGM scale. For instance, The COSMOS Lyman-Alpha Mapping And Tomography Observations (CLAMATO) survey with Keck/LRIS (Lee et al. 2014) and the Prime Focus Spectrograph-Subaru strategic program (PFS SSP) Galaxy Evolution survey (Greene et al. 2022) have a few Mpc transverse resolution at $z > 1$. Higher spatial resolutions can be achieved using QSO pairs (e.g., Tytler et al. 2009; Urbano Stawinski et al. 2023), gravitationally lensed QSOs (e.g., Chen et al. 2014; Rubin et al. 2018), and gravitational-arcs as background sources (e.g., Lopez et al. 2018). A galaxy-centered stacking approach is also useful to statistically map gas and metals with impact parameters ranging from ≈ 50 kpc to a few Mpc (e.g., Rakic et al. 2012; Turner et al. 2014; Dutta et al. 2024). Recently, Bordoloi et al. (2023) achieves the impact parameters of ≈ 20 – 300 kpc individually, using James Web Space Telescope (JWST)/NIRCam slitless grism spectroscopy. These studies enable to reach an outer-CGM scale, but an inner-CGM scale is difficult to investigate. Moreover, the identification of the host galaxies that are responsible for the absorption lines in QSO spectra is a challenging task. Hence, this method cannot provide the spatial distribution of gas and metals around individual host galaxies on an inner CGM scale.

A complementary method to absorption-line studies is direct observations of the CGM in emission, which has been challenging because of its low surface brightness (SBs). Modern optical integral field units (IFUs) such as the Multi-Unit Spectroscopic Explorer (MUSE; Bacon et al. 2010) and the Keck Cosmic Web Imager (KCWI; Morrissey 2018) make it possible to detect diffuse CGM emission around individual host galaxies (e.g., Wisotzki et al. 2016). In particular, extended Ly α emission, the so-called “Ly α halo”, which traces cool and warm hydrogen CGM (e.g., Steidel et al. 2011; Momose et al. 2014; Guo et al. 2023c) has been intensively detected and studied around individual Ly α emitters (LAEs) at $z \approx 2$ – 6 (e.g., Leclercq et al. 2017, 2020; Chen et al. 2021; Claeysens et al. 2022; Erb et al. 2023). Their diverse profiles and statistical trends as well as origins can now be discussed. Recently, a high fraction of Ly α halos around UV-continuum selected (not based on Ly α) galaxies at $z \sim 3$ – 4 is reported (Kusakabe et al. 2022). The ubiquitous presence of reservoirs of hydrogen in the CGM is directly confirmed at cosmic noon and earlier epochs ($z > 3$ with MUSE).

However, metals in the CGM at cosmic noon ($z \sim 2$ – 4), which is the peak of star-forming activity of galaxies, have not been directly confirmed in emission, in particular for the cool phase. The CGM is known to be metal enriched even at $z \sim 2$ – 4 from transverse absorption-line studies (e.g., Turner et al. 2014; Lehner et al. 2016; Méndez-Hernández et al. 2022; Urbano Stawinski et al. 2023; Bordoloi et al. 2023). This is also suggested by outflowing metals identified by down-the-barrel analysis (e.g., Shapley et al. 2003; Steidel et al. 2010; Du et al. 2018; Sugahara et al. 2017) and by broad-line components seen in spectra (e.g., Carniani et al. 2023; Xu et al. 2023). A popu-

lar emission tracer of cool metal-enriched CGM, Mg II $\lambda\lambda 2796, 2803$, is useful only at $z \lesssim 2$ because at higher redshifts the observed wavelength shifts into the near-infrared and the cosmic dimming effect is more severe (e.g., Rubin et al. 2011; Erb et al. 2012; Martin et al. 2013; Burchett et al. 2021; Zabl et al. 2021; Leclercq et al. 2022; Dutta et al. 2023; Guo et al. 2023a, Pessa et al. 2024 in prep.). Other possible tracers are [O II] $\lambda\lambda 3726, 3729$ (e.g., Yuma et al. 2013, 2017; Epinat et al. 2018; Johnson et al. 2018) and very faint Fe II* $\lambda\lambda 2365, \lambda\lambda 2396, \lambda\lambda 2612, \text{ and } \lambda\lambda 2626$ (e.g., Finley et al. 2017; Shaban et al. 2022). At $z \approx 4$ – 7 , [C II] $\lambda 158 \mu\text{m}$ can be covered by sensitive ALMA bands 6 and 7 ([C II] halos; e.g., Fujimoto et al. 2019; Ginolfi et al. 2020). At $z \approx 2$ – 4 , no bright emission tracer of the cool metal-enriched CGM is available in the observed optical regime. While extremely faint, the most promising tracers are the emission lines Si II* $\lambda\lambda 1265, 1309, 1533$, which are not contaminated by other line features at nearby wavelengths given the spectral resolution of current facilities (cf. C II* $\lambda 1335$ emission and C II $\lambda 1334$ absorption, which cannot be resolved by the resolving power of MUSE, ≈ 3000).

Si II* are fine-structure fluorescent emission lines from singly ionized silicon, which is a low-ionization state (LIS), with an ionization energy close to H I (ionization energy for Si and Si⁺ are 8.1 eV and 16.4 eV, respectively). The energy levels of the Si⁺ ion for the three transitions this paper focuses on are shown in Figure 1. The origin of Si II* is suggested to be “continuum pumping” (or “continuum fluorescence”) rather than collisional excitation or recombination (Shapley et al. 2003). Collisional excitations are dominant only in dense environments with high electron densities, which is higher than typical values in H II regions (Shapley et al. 2003). And the recombination rates of Si²⁺ into the excited Si⁺ is of the same order as the collisional excitation rates when Si⁺ and Si²⁺ have comparable abundance with $T \sim 10^4$ K (Shull & van Steenberg 1982; Shapley et al. 2003). Shapley et al. (2003) model observed nebular emission lines using the photoionization code CLOUDY (Ferland et al. 1998). They find that any model that reproduces the line ratios of the other lines ([O III], [O II], H β , O III], and C III]) predict more than one order of magnitude weaker Si II* emission by collisions and recombination. Therefore, those two processes are unlikely to be the dominant origin of Si II* emission in H II regions. As for the continuum pumping scenario, first, Si⁺ in neutral clouds absorbs the UV continuum and creates Si II resonant absorption features. Second, a fraction of Si⁺ deexcites to the fine-structure level and emits Si II* photons (see Figure 1). Si II* lines are escape channels of resonant transitions and are expected to be as spatially extended as the resonant emission lines.

Fluorescent lines are extremely faint, and Si II* emission is ~ 10 – 50 times weaker than Ly α emission of LAEs (Steidel et al. 2018). In fact, extended Si II* emission has not been directly detected. Wang et al. (2020) found weak Si II* emission lines compared to the associated absorption line in HST/Cosmic Origins Spectrograph (COS) data for 5 galaxies at $z = 0$, which implies that the bulk of Si II* emission arises on larger scales than the COS aperture. Gazagnes et al. (2023) compare COS spectra of Si II* $\lambda 1265$ for 45 local galaxies (COS Legacy Archive Spectroscopic Survey, CLASSY) with mock spectra from zoom-in simulations (Mauerhofer et al. 2021). They find stronger Si II* emission lines in the simulations than observed, and they argue that aperture losses of COS can explain the weakness of observed Si II* and that Si II* $\lambda 1265$ is spatially extended. Very recently, Vasan G. C. et al. (2024) study spatially-resolved outflow properties for a lensed star-forming galaxy at $z = 1.87$ with KCWI and show that Si II* emission is more extended than the continuum for a certain direction extracted with a pseudo slit.

In this project, we search for Si II* halos around galaxies at cosmic noon (at $z = 2-4$) as a tracer of metal-enriched cool CGM using integral field unit data to remedy the problem. We use data from the MUSE Hubble Ultra Deep Field (HUDF) survey (Bacon et al. 2023) and test the presence of Si II* halos with surface brightness profiles of Si II* and UV continuum. We report the first detections of Si II* halos. We also stack the MUSE data for a UV-bright subsample to study the general extent of Si II* and compare it with simulations.

The paper is organized as follows. In Section 2, we describe the data and the sample construction. Section 3 presents methods and results of the search for individual Si II* halos and those of a stacked subsample. In Section 4, we discuss photon conservation for Si II, compare observed results with those of zoom-in simulations, and discuss how to increase a sample size with different selection criteria. Finally, conclusions are given in Section 5. Throughout this paper, we assume the Planck 2018 cosmological model (Planck Collaboration et al. 2020) with a matter density of $\Omega_m = 0.315$, a dark energy density of $\Omega_\Lambda = 0.685$, and a Hubble constant of $H_0 = 67.4 \text{ km s}^{-1} \text{ Mpc}^{-1}$ ($h_{100} = 0.67$). Magnitudes are given in the AB system (Oke & Gunn 1983). All distances are in physical units (kpc), unless otherwise stated.

2. Data and sample

To search for extended Si II* emission of $z \gtrsim 2$ galaxies, we utilize deep MUSE data from data release 2 (DR2) of the MUSE HUDF surveys (Bacon et al. 2023), where rich multi-wavelength data are also available (see Section 2.1). We construct our sample with the DR2 catalog using the systemic redshifts for the individual search and stacking analyses (see Sections 2.2 and 2.3). We create masks to avoid potential contaminations from neighboring galaxies (see Section 2.4).

2.1. Data and catalogs

The MUSE HUDF DR2 data are obtained as a part of the MUSE guaranteed time observations (GTO) program described in Bacon et al. (2023). We use two fields among the MUSE HUDF DR2 data set: a single $1 \times 1 \text{ arcmin}^2$ pointing with a 31-hour depth (udf-10, see also Bacon et al. 2017 and Inami et al. 2017), and the adaptive-optics (AO) assisted MUSE eXtremely Deep Field (mxdf), whose maximum integration time is 141 hours with a 1-arcmin diameter field of view. They are located inside the *Hubble* eXtreme Deep Field (XDF; Illingworth et al. 2013) with deep HST data (see Bacon et al. 2023, for more details). The udf-10 covers the optical wavelength range from 4750 Å to 9350 Å, while mxdf covers from 4700 Å to 9350 Å, with an AO gap from 5800 Å to 5966.25 Å. The spectral resolving power of MUSE varies from $R = 1610$ to 3750 at 4700 Å to 9350 Å, respectively. The full width at half maximums (FWHMs) of the Moffat point spread function (Moffat PSF, Moffat 1969) are $0''.7$ ($0''.7$) at the blue wavelength edge and $0''.5$ ($0''.6$) at the red wavelength edge for the mxdf (udf-10). The 3σ point-source flux limit for an unresolved emission line in the mxdf (the udf-10) is $\approx 6 \times 10^{-20} \text{ erg s}^{-1} \text{ cm}^{-2}$ ($\approx 2 \times 10^{-19} \text{ erg s}^{-1} \text{ cm}^{-2}$), at around 7000 Å (not affected by OH sky emission), which corresponds to a 3σ surface brightness limit for an unresolved emission line of $\approx 1 \times 10^{-19} \text{ erg s}^{-1} \text{ cm}^{-2} \text{ arcsec}^{-2}$ ($\approx 2 \times 10^{-19} \text{ erg s}^{-1} \text{ cm}^{-2} \text{ arcsec}^{-2}$, see Bacon et al. 2023).

The MUSE HUDF DR2 catalog includes 2221 sources from $z = 0$ to 6.7, which are selected by emission-line detections as well as through HST priors. The details of the catalog construc-

tion are described in Bacon et al. (2023). Each MUSE object has a source file, which is in the format of MPDAF¹ multi-fits format and is composed of various data files such as minicubes, images, and spectra. It is available on the AMUSED website². We use $5'' \times 5''$ minicubes from each of the source files. We create continuum-subtracted minicubes following the method used in Kusakabe et al. (2022), taking the median for each pixel within a spectral window of 100 slices (masking $\pm 400 \text{ km s}^{-1}$ around the Ly α wavelength if the spectrum covers). The continuum subtraction is useful not only to investigate emission lines, but also to remove neighboring sources around a target source. In order to identify HST counterparts, calculate UV magnitudes, and create masks, we use the HST catalog and data from Rafelski et al. (2015).

2.2. Sample selection

We construct a sample of galaxies at $z = 2.07-3.87$, for which the [C III] $\lambda 1907$, C III] $\lambda 1909$ doublet nebular lines and at least one of the Si II* $\lambda 1265$, 1309, 1533 lines are redshifted into the MUSE wavelength range. The available redshift ranges for the three Si II* lines are shown in the top panel in Figure 2. We require sources to have a secure spectroscopic redshift with $ZCONF \geq 2$ and a C III] signal-to-noise ratio (SNR) of $SNR > 3$. We visually inspect C III] in spectra and images extracted from MUSE cubes to ensure these criteria. We use systemic redshifts measured by the C III] line rather than reference redshifts (REFZs) in the DR2 catalog, which are given by Ly α at $z \gtrsim 3$ or absorption lines at $z \approx 2$. Si II* lines are expected to be located at the systemic redshifts (e.g., France et al. 2010; Dessauges-Zavadsky et al. 2010; Jaskot & Oey 2014; Wang et al. 2020), though redshifted Si II* lines are also reported, which could be due to the contamination of the absorption at the blue edge for low-resolution spectra or stacking of spectra for different sources (e.g., Shapley et al. 2003; Erb et al. 2010; Berry et al. 2012). As Si II* lines are extremely faint, secure measurements of systemic redshifts enable us to not rely on the presence of Si II* in 1D spectra on a galaxy scale and to directly search for spatially extended Si II* in narrowband images extracted from MUSE cubes. We limit our sample to galaxies with a secure and isolated HST counterpart (based on Rafelski et al. 2015, MAG_SRC=RAF) with a high HST matching confidence level of $MCONF \geq 3$ in the DR2 catalog. In total, we have 39 galaxies, whose absolute UV magnitudes (M_{UV}) and systemic redshifts (z_{sys}) are shown in the bottom panel of Figure 2. The M_{UV} is calculated at rest-frame 1600 Å by fitting 2 or 3 HST bands with a power-law model (with parameters being an amplitude and a UV slope β).

We would like to note that our sample is constructed simply with the deepest data for this pilot study. We discuss possible strategies to extend the sample in Section 4.3.

2.3. Stacked sample

The subsample used for the stacking analysis is restricted to bright UV-continuum galaxies using an apparent magnitude cut of $m_{UV} = 26.0$, in order to enhance the SNR of the stacked images (see Section 3.3 and Figure 2). The origin of Si II* is predicted to be continuum pumping as mentioned in Section 1, and a bright UV continuum is necessary to have a bright Si II* emission line. Indeed, Si II* emission lines are stronger in 1D stacked spectra for subsamples of MUSE LAEs with brighter UV contin-

¹ <https://mpdaf.readthedocs.io/en/latest/>

² <https://amused.univ-lyon1.fr/>

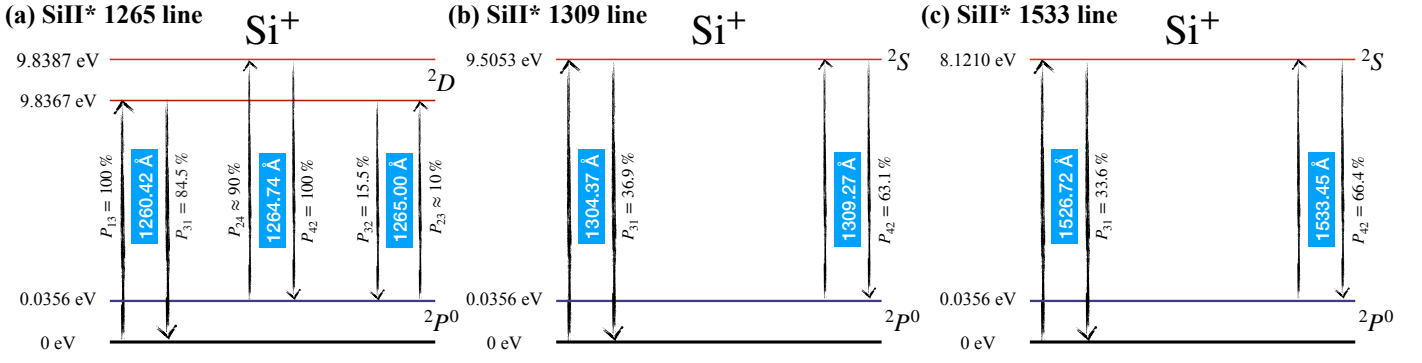


Fig. 1. Energy levels of Si⁺ ions and different channels of excitation and de-excitation from the ground-state or the fine-structure level (fluorescence) for Si II* λ 1265, 1309, 1533 lines in panels (a) to (c), respectively. The probabilities (P) of related transitions and their wavelengths are also shown.

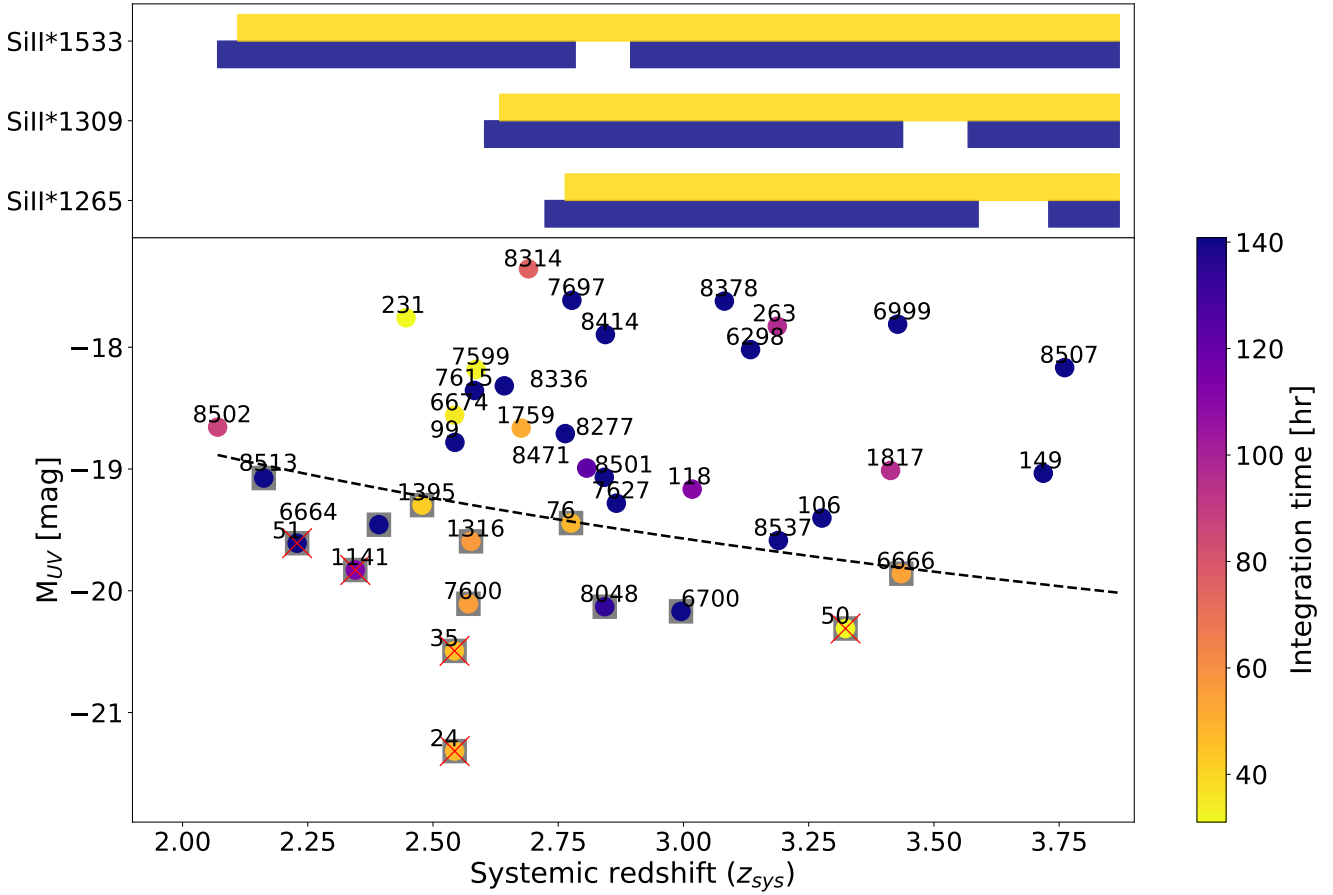


Fig. 2. Redshift distribution of our sample. (Top) Redshift ranges covered for the Si II* λ 1265, 1309, 1533 lines. Navy and yellow shades indicate mxf and udf-10, respectively. (Bottom) The M_{UV} and z_{sys} distribution of our sample with MUSE IDs. The color bar indicates the integration time. The stacked subsample is enclosed by gray squares. The M_{UV} corresponding to $m_{UV} = 26.0$ (magnitude cut for the stacking sample) at each redshift is shown by the black dashed line. The individually-detected Si II* halos are indicated by red crosses (see Section 3.2).

uum (such as those with higher stellar masses and with brighter UV magnitudes) than the subsample counterparts in Feltre et al. (2020). The number of sources for the stacking subsample is 14. We would like to note that applying fainter magnitude cuts indeed reduces the SNRs of the Si II* lines.

2.4. Masks

In order to exclude pixels that might be affected by bright neighboring objects in Si II* narrowband images extracted from the

minicubes, we create neighboring object masks. First, we define target pixels. We use an HST segmentation map and mask pixels not corresponding to a main target on a 5'' \times 5'' HST/F775W cutout for each object. It is convolved with the MUSE mof-fat PSF at the redshifted Si II* wavelength for the main target and rebinned to match the MUSE pixel scale. Then, we apply a threshold value of 0.1 to the peak-normalized convolved cutout to delimit the spaxels of the target. Lower threshold values such as 0.05 cause contamination of neighboring objects inside the target spaxels. Using a higher threshold value of 0.2 does not

change the main results in this paper but enhances the contaminated pixels outside the following neighboring object masks. Therefore, we adopt the value 0.1.

Second, we use a $5'' \times 5''$ HST/F775W cutout whose sky and the main target are masked with the HST segmentation map for each source. This cutout is convolved with the MUSE PSF and rebinned to match the MUSE pixel scale. Then, we define pixels brighter than a certain threshold on the cutout, except for the target pixels, as masked pixels. The applied threshold value is half of the value above in the absolute sense (without normalization).

3. Results

3.1. Extracted images and surface brightness profiles

For each source, we create a Si II* emission narrowband (NB) image from the continuum-subtracted minicube. We sum fluxes in a window of $\pm 200 \text{ km s}^{-1}$ around the Si II* wavelength, excluding NaN (masked) spaxels, wavelength slices affected by OH skylines, and the AO gap in the cube. The variance image of the NB is created from that of the cube with error propagation. A UV continuum broadband (BB) is created from the median filtered original minicube with a window of ± 300 wavelength slices (375 \AA) around the Si II* wavelength (masking below $+400 \text{ km s}^{-1}$ from the Ly α wavelength) to obtain a good SNR. We also exclude NaN in the cube and the AO gap. If the wavelength window is not fully covered, we use as many spectral slices as possible. The variance image of the BB is assumed to be identical to that of the mean-filtered BB created from the same cube with error propagation. We apply a neighboring object mask (see Section 2.4) and measure SB profiles of these two bands using PHOTUTILS (Bradley et al. 2021). The aperture and annuli are centered at the HST counterpart position with 1-pixel ($0''.2$) annuli from $0''.1$ to $0''.9$ and then 2-pixel annuli at $1''.2$ and $1''.6$, followed by a 3.5-pixel annulus at $2''.15$, to enhance the SNR at outer radii. The azimuthally-averaged radial SB profiles are calculated from the effective areas and the measured flux above. We normalize the SB profile of the UV continuum at the center ($R = 0$) to that of Si II*.

The top panels in Figure 3 show the Si II* emission NB, the UV-continuum BB, and the SB profile for a highlighted object, MID= 1141. The details of this object are explained later (Section 3.2).

3.2. Identification of Si II* halos

To identify extended Si II* emission, we compare the shape of the azimuthally-averaged radial SB profiles of the UV continuum and the Si II* emission. We take account of uncertainties in SB profiles of Si II* emission only (blue shades in Figure 3) as those of UV continuum are negligibly small (gray shades). If more than two adjacent data points of the Si II* SB profiles deviate by more than 1σ from the normalized continuum, we identify it as extended Si II*. The significance of the presence of the halo with this criterion corresponds to more than $97.5\%^3$. We would like to note that, as we use circular photometry, our test may miss non-circular halos as discussed in Kusakabe et al. (2022) for Ly α halos. Our halo search is not complete in that sense but secure.

³ The probability for two adjacent data points with $> 1\sigma$, which is caused by chance due to noises (i.e., fake detections), is $(\frac{1-0.6826}{2})^2 = 2.5\%$ with an assumption that noises follow the normal distribution.

Among the 39 sources, we detect five Si II* halos for the Si II* λ 1533 line (MID= 24, 35, 50, 51, 1141; see Figure 3). These are the first detections of individual Si II* halos. The Si II* lines in the DR2 reference spectra show that there are no significant velocity shifts for the line peaks of Si II* λ 1533 (Figure 3; the systemic redshifts are given by the [C III] λ 1907, C III] λ 1909 doublet nebular lines, see Section 2.2).

Among the five Si II* halo sources, MID=1141, shown in the top panels of Figure 3, is the best-case object. The Si II* emission profile shows three data points that deviate by more than 1σ from the normalized continuum. This object is well-isolated and without a spatial offset of Si II* from the UV continuum. The images are not significantly affected by masks, which makes the SB profile test secure. The Si II* emission line can be clearly confirmed on the spectrum shown in Figure 3. MID= 24 and MID=35 are a pair of galaxies, which could contaminate each other's $5'' \times 5''$ images despite the neighboring object mask. Moreover, MID=35 is an X-ray detected AGN (Luo et al. 2017), whose Si II* halo might have a different origin from other sources. The Si II* NB of MID=50 shows a peak offset from the UV center measured with the HST data, with two neighboring LAEs in the DR2 catalog, which spatially overlap with the extended Si II* emission. The Si II* SB of MID=51 is noisy even though it meets our halo criterion. Considering these details on the five sources, we highlight MID=1141 in the following sections.

The redshifts of the individually-detected Si II* λ 1533 halos range from 2.23 to 3.32 with four of them at $z_{\text{sys}} \leq 2.5$. The non-detections at $z > 3.5$ could be due to the high noise levels of MUSE data at red wavelengths (severe night sky and low sensitivity; Bacon et al. 2023) and the cosmic dimming effect on the SB profiles (by a factor of 2.7 between $z = 2.5$ and $z = 3.5$).

Another interesting result is that we cannot confirm extended emission for any of the other Si II* lines (λ 1265, 1309). In the optically thin limit, the strengths of fluorescent lines are expected to depend on the strength of the paired absorption lines, which are determined by their oscillator strengths, f . In particular, the Si II λ 1260 resonant absorption line corresponding to the Si II* λ 1265 line has a ten times larger f than that of the Si II λ 1526 resonant absorption line corresponding to the Si II* λ 1533. However, in the simulations of Mauerhofer et al. (2021) there is no significant difference in the equivalent widths of Si II* λ 1265 and Si II* λ 1533 absorption lines because both lines are saturated (Mauerhofer et al. in prep.). In such an optically thick regime, the equivalent widths for the corresponding fluorescent emission (Si II* λ 1265 and Si II* λ 1533) are similar in the simulations. Therefore, non-detections of Si II* λ 1265 as well as Si II* λ 1309 would not be due to fainter total fluxes for these lines than for the 1533 line. The reason for nondetections of Si II* λ 1265 and Si II* λ 1309 halos are not clear. The samples for Si II* λ 1265, 1309 lines are limited to high redshifts ($z_{\text{sys}} > 2.8$ and > 2.6 , respectively), and none of them are bright in apparent UV magnitudes, which are directly related to SNRs (see Figure 2). Bright sources would be crucial for the detection of diffuse Si II* lines if the origin of Si II* is continuum pumping. However, we cannot distinguish whether it is caused by differences in lines, samples, or noise levels. We note that the Si II* λ 1533 lines are also brighter than the other two lines in the stacked MUSE LAE spectra of Feltre et al. (2020) and Kramarenko et al. (2023), which might also be due to the difference in objects stacked for different Si II* lines.

One of the individually-detected objects, MID=50 at $z_{\text{sys}} = 3.32$, has 3 Si II* lines covered with MUSE. We coadd the NBs and BBs for the 3 Si II* lines by taking the median (with the same method as used in Section 3.3) and show them in the fifth row of

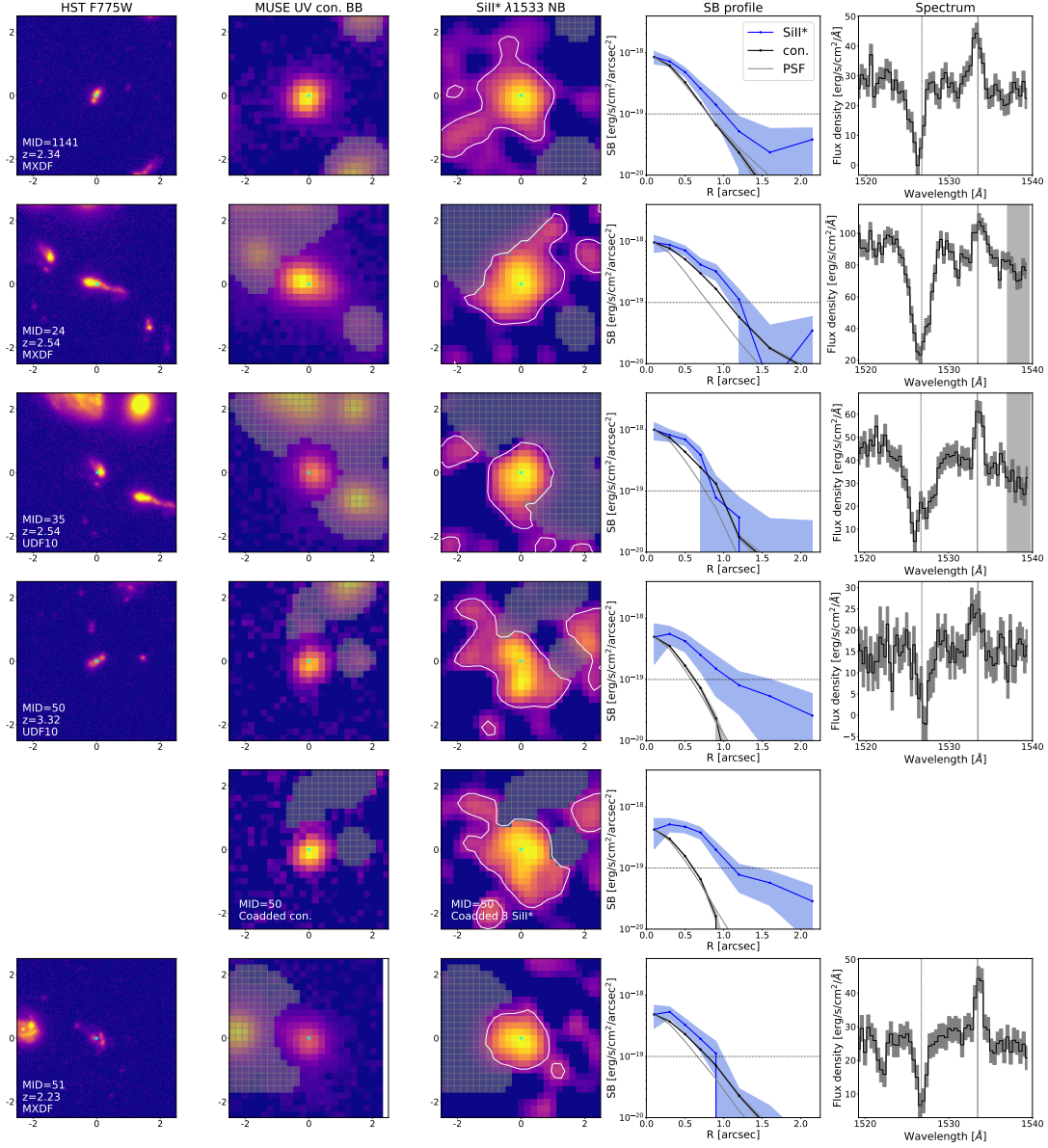


Fig. 3. (From left to right) The HST image, MUSE UV-continuum BB image, MUSE Si π^* NB image, SB profile, and Si π^* spectrum for the five sources with Si π^* halo detections. Each row except the fifth shows the Si π^* 1533 line for a different object. The fifth row shows a coadded result of three Si π^* lines for MID=50 at $z = 3.32$, whose three Si π^* lines (Si π^* λ 1265, Si π^* λ 1309, and Si π^* λ 1533) are covered with MUSE. The image size is five arcsec. Gray shades on the images indicate masked spaxels. For presentation purposes, NB images are smoothed with a Gaussian kernel with $\sigma = 1.5$ spaxel. White contours correspond to 1×10^{-19} erg s $^{-1}$ cm $^{-2}$ arcsec $^{-2}$ (the typical 3σ SB limit of the NBs in MXDF for an unresolved emission Bacon et al. 2023). Cyan crosses on images indicate the HST center. The SB profiles of the UV continuum shown by black lines are normalized at the center ($R = 0$) to the SB profiles of Si π^* shown by blue lines. Blue and gray shades represent 1σ uncertainties of the SB for Si π^* emission and UV continuum, respectively. Gray solid and dotted lines show the SB profile of the PSF normalized at the center and the typical 3σ SB limit of the NBs in MXDF for unresolved emission, respectively. The rest-frame “reference spectrum” and its 1σ uncertainty are shown by a black solid and a gray shade, respectively. The reference spectrum for each object is chosen from those extracted by five different methods to have high-SNR in Bacon et al. (2023). The wavelengths for Si π^* emission and Si π absorption lines are indicated by gray solid and dotted lines, respectively. MID= 24 and MID= 35 have broad C IV λ 1548, 1550 lines, which are masked by gray shades at the red edge of the spectrum.

Figure 3. Extended Si π^* is confirmed with a better SNR, which implies the Si π^* λ 1265, 1309 lines are also spatially extended.

3.3. Stacking analysis

To test the general presence of Si π^* halos, we stack 14 UV-bright sources (see Section 2.3). The numbers of sources with the magnitude cut of $m_{UV} = 26.0$ available for each of the Si π^* λ 1265, 1309, 1533 lines are five, four, and 13, respectively,

which are limited by the MUSE wavelength coverage and the AO gap (see Figure 2)⁴. Therefore, we only stack a subsample for the Si π^* λ 1533 line and take the mean and median of the Si π^* NBs and BBs without weighting, while masking neighboring objects. We also stack 14 sources by combining the NBs and BBs for the

⁴ The MIDs for the Si π^* λ 1265 subsample are 50, 76, 6666, 6700, and 8048. Those for the Si π^* λ 1309 are 50, 76, 6700, and 8048. Those for the Si π^* λ 1533 are 24, 35, 50, 51, 76, 1141, 1316, 1395, 6664, 6666, 6700, 7600, and 8513.

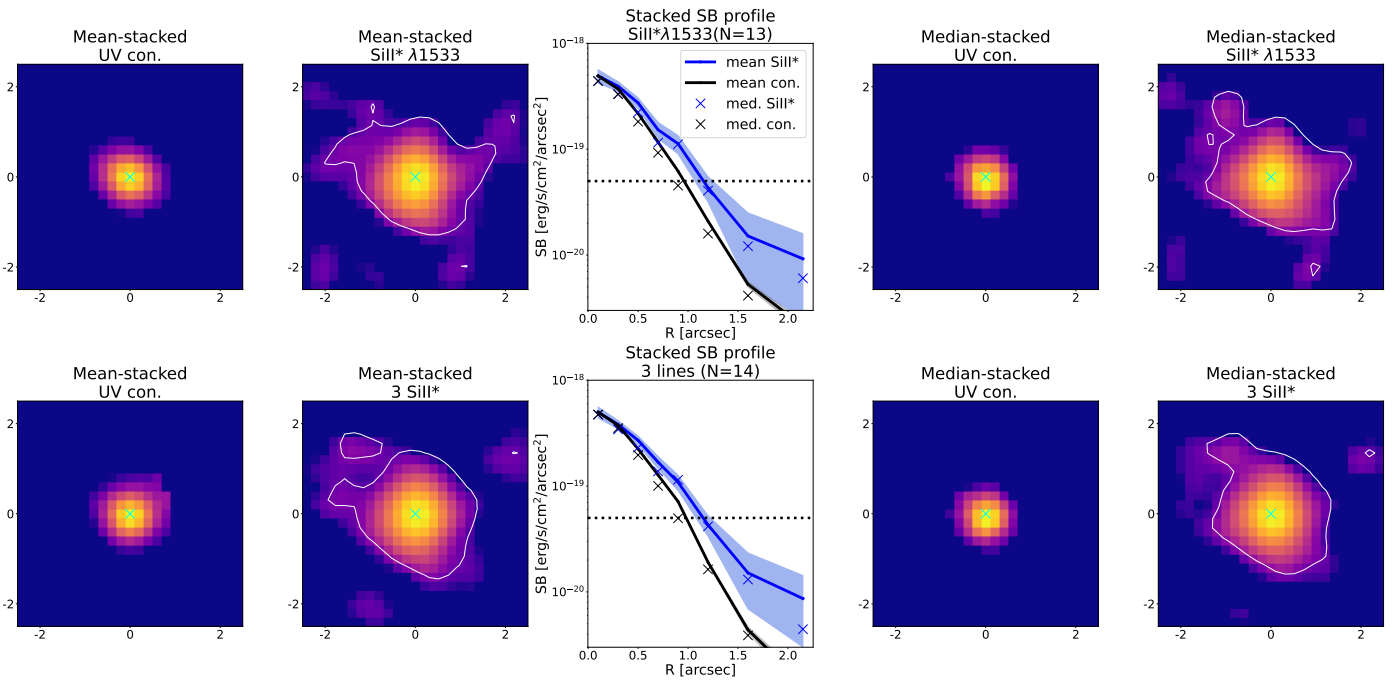


Fig. 4. Stacking results. From left to right, we show the mean-stacked UV continuum image, the mean-stacked Si II* emission image (5 arcsec each), the mean surface brightness profiles, the median-stacked UV continuum image, and the median-stacked Si II* emission image. Top and bottom panels represent stacking results of the Si II* λ 1533 line ($N=13$) and those of all Si II* lines (22 images for 14 sources), respectively. Cyan crosses on images indicate the HST center. White contours correspond to $5 \times 10^{-20} \text{ erg s}^{-1} \text{ cm}^{-2} \text{ arcsec}^{-2}$ which is also shown by black dotted lines on the SB profiles. The SB profiles of the mean-stacked Si II* and UV continuum are indicated by the blue and black lines, respectively, while the median-stacked Si II* and UV continuum are shown by the blue and black crosses, respectively. The blue and gray shades represent 1σ uncertainties of the SB for Si II* emission and UV continuum, respectively. Following Figure 3, SB profiles for the continuum are normalized at the center ($R=0$) to those for Si II* emission.

three lines. The variance images for the mean stacking, which we use for our halo test, are created based on error propagation. Then, we apply the SB profile test for the mean-stacked images with the same method as used in Sections 3.1 and 3.2, as the uncertainties can be calculated correctly for the mean but not for the median.

The results of this stacking experiment are shown in Figure 4. As shown in the top row, we confirm the existence of a Si II* λ 1533 halo with five data points that deviate by more than 1σ from the normalized continuum profile. The median profile of Si II* λ 1533 is consistent with the mean profile and deviates from the median continuum as well, in particular at large radii. These tests may suggest that the detected halo in the mean profile is not dominated by a few extreme objects. This is the first secure detection of a stacked Si II* halo. It may imply that the individually detected sources are not extreme cases, Si II* halos must be common for UV-bright galaxies at $z = 2-4$.

The bottom row of Figure 4 shows the results of stacking all the Si II* narrowbands and corresponding UV continuum bands for the 14 sources (three lines; in total 22 images). We find that the mean-stacked Si II* deviates by more than 1σ from the mean-stacked UV continuum for six data points. The median-stacked Si II* is consistent with the mean-stacked Si II*, and the deviation from the normalized continuum is similarly seen with the median-stacked profiles.

We note that removing MID= 35, which is an X-ray detected AGN with extended Si II* (see Section 3.2), does not change the results and that the other 13 sources do not have a counterpart in the deep X-ray catalog (Luo et al. 2017). We also note that stacking without individually-detected Si II* halos results in nondetections of extended Si II*. As shown in Figure 2, all

the individually-detected sources have a bright M_{UV} (and also a bright m_{UV}) and are located at relatively low redshifts. It is not surprising that removing such five sources results in nondetections. If the origin of the Si II* is continuum pumping, as we expect, it then should be more challenging to detect Si II* halos without these bright sources. We also stack various subsamples including all the sources without individually-detected halos and get nondetections of extended Si II* emission. Future instruments such as BlueMUSE (Richard et al. 2019) or a larger sample compiling MUSE and KCWI archive data will allow us to investigate the dependence of Si II* halos on sample properties such as M_{UV} (see Section 4.3). It will enable us to draw a firm conclusion of whether Si II* halos are indeed common for UV-bright galaxies at $z = 2-4$ or not.

4. Discussion

4.1. Testing photon conservation

Shapley et al. (2003) suggest that the origin of the Si II* is continuum pumping (see Section 1 for other origins). For the Si II* λ 1533 line, Si⁺ in neutral clouds makes a Si II λ 1526 resonant absorption line, and then a fraction of Si⁺ deexcites to the fine-structure level, emitting Si II fluorescence photons at 1533 Å (see Figure 1). As the Si II is a resonant line, the Si II* line can be regarded as an escape channel of photons from resonant scattering. If dust extinction is negligible and the escape is isotropic, then the equivalent width (EW) of Si II* emission and that of the corresponding resonant absorption should be comparable because of photon conservation. However, it is possible for the absorption and emission to have different EWs for one given di-

rection of observations even if the origin is continuum pumping without dust, because of the complex gas distribution in front of stars in galaxies (e.g., Prochaska et al. 2011b; Carr et al. 2018). Simulations predict that absorption lines depend sensitively on the direction of observations (Mauerhofer et al. 2021; Gazagnes et al. 2023). Below, we assume an isotropic case.

To investigate the scenario of continuum pumping, we use the isolated, high-SN object MID= 1141 (see Section 3.2) and test photon conservation between Si II absorption and associated Si II* emission, which is commonly assessed with the EWs of these lines (e.g., Prochaska et al. 2011a; Wang et al. 2020). First, we check the flux curve of growth (CoG) for the continuum and the emission line to determine the spatial extent. Second, we measure the EW curve of growth for Si II* emission and compare it with the absorption EW. We measure EWs from the MUSE data (without HST), which makes the EW comparison fair. Ideally, we should measure the curve of growth for the absorption. However, due to the limited depth and spatial resolution of our data, we have to assume that the absorption follows the same spatial profile as that of the continuum. The left panel of Figure 5 shows normalized fluxes within growing apertures for continuum (black) and Si II* λ 1533 (blue). Fluxes are measured from the Si II* λ 1533 NB image and the corresponding UV continuum BB image (Section 3.1) with PHOTUTILS and the neighboring object mask with corrections of masked areas. On a galaxy-scale of $R= 0''.8$, the aperture includes about 80% of the continuum but only 50% of the Si II*. An $R= 2''.4$ aperture captures most of the Si II* flux.

The right panel shows rest-frame EWs for Si II* λ 1533 emission within growing apertures (blue), compared with the EW for Si II λ 1526 absorption measured at $R\leq 0''.8$, $EW_{\text{abs}}(\text{Si II}\lambda 1526)= 1.6 \pm 0.2 \text{ \AA}$ (red). Rest-frame EWs are measured in spectra extracted from the original minicube (to which the neighboring object mask is applied) with growing apertures. The continuum flux density is measured by the median filtering each spectrum from 50-slice shorter wavelength (62.5\AA) than the absorption to 50-slice longer wavelength than the emission. Absorption and emission fluxes are measured as differences from the continuum. The EW for Si II* λ 1533 is $EW_{\text{em}}(\text{Si II}^*\lambda 1533)= 1.1 \pm 0.1 \text{ \AA}$ at $R\leq 0''.8$, which is smaller than $EW_{\text{abs}}(\text{Si II}\lambda 1526)= 1.6 \pm 0.2 \text{ \AA}$. $EW_{\text{em}}(\text{Si II}^*\lambda 1533)$ increases with R and reaches $EW_{\text{em}}(\text{Si II}^*\lambda 1533)= 1.8 \pm 0.4 \text{ \AA}$ at $R\leq 2''.4$, which is consistent with $EW_{\text{abs}}(\text{Si II}\lambda 1526)$ at $R\leq 0''.8$ within the 1σ uncertainties (see Figure 6 for the spectra), although the EWs have large measurement errors. Therefore, the absorption EW on the galaxy scale and the fluorescent emission EW on the CGM scale are consistent with each other. This is compatible with photon conservation on the CGM scale, albeit with large uncertainties. It implies that the origin of extended Si II* emission can be the continuum pumping as predicted under the assumption of isotropic escape and no dust. In that case, either a small amount of dust, a low optical depth, or a combination of both are implied. Unfortunately, data for the other four sources with individual Si II* halos are either noisy or have accompanying galaxies inside their $5''\times 5''$ minicubes, which prevents us from obtaining a firm conclusion about the mechanisms for the four sources. The trend of increasing EW of Si II* emission with radius beyond the galaxy scale is predicted by simulations (Mauerhofer et al. 2021), which are compared with slit spectroscopy of low-redshift galaxies in Gazagnes et al. (2023, see also Wang et al. 2020).

4.2. Comparisons with zoom simulations

We compare our stacked Si II* λ 1533 profile with those from the cosmological zoom-in simulations of Mauerhofer et al. (2021), which are used in Gazagnes et al. (2023) and Blaizot et al. (2023). Mauerhofer et al. (2021) present three snapshots containing a relatively small galaxy (such as MUSE LAEs) at $z = 3.0, 3.1,$ and 3.2 . The stellar mass for the galaxy is $\sim 2 \times 10^9 M_{\odot}$, and the star formation rate ranges from ~ 2 to $5 M_{\odot} \text{ yr}^{-1}$ for the three snapshots. Si II* photons in this simulations originate from continuum pumping. We provide mock MUSE cubes for observations from 12 directions for each snapshot in the rest frame. This original mock cube has a size of $300 \times 300 \times 110$ pixels corresponding to $7''.5 \times 7''.5 \times 16.6 \text{ \AA}$ (from 1521.83 \AA to 1538.42 \AA) with a spaxel scale of $0''.025/\text{pix}$. Then, to match the size of observed and simulated galaxies, we measure the median size of the simulated galaxy among the 36 directions. A UV-continuum BB image is created from each median-filtered original cube with a window from 1528.5 \AA to 1531.5 \AA (the continuum between Si II absorption and Si II* emission). We define the galaxy center by identifying the brightest pixel, as in Gazagnes et al. (2023), for each UV continuum BB image after HST PSF convolution (F606W in Rafelski et al. 2015). The half-light radius (R_{50}) is measured around the galaxy center with the original mock cube (without HST PSF convolution) using PHOTUTILS. The median R_{50} for the simulated galaxy is $0''.0875$ (3.5 pix). This is 1.7 times smaller than the median R_{50} for the 14 stacked galaxies ($R_{50}=0''.15$ with F606W after PSF correction). Since we do not have a simulated galaxy that is large enough in Mauerhofer et al. (2021), we manually rescale the original mock cube by a factor of 1.7 by interpreting the spaxel scale as $0''.0425/\text{pix}$, which is referred to as an intrinsic mock cube below. The intrinsic mock cubes are cut out around the galaxy center defined above and are 5 arcsec each. The $5''$ cubes are convolved with the MUSE PSF and line spread function (LSF) described in Bacon et al. (2023) at the median redshift of the stacked sample ($z = 2.68$). Then the convolved mock cubes are rebinned to match the MUSE cubes in the rest frame. We apply similar analyses to the 36 mock MUSE cubes as used for the observational data (see Section 3). A slight difference from the method for the MUSE data is continuum subtraction. Continuum cubes used for continuum subtraction are created using median filtering from 1528.5 \AA to 1531.5 \AA which are also used for the UV-continuum BB images. The 1σ uncertainties for stacked mock data are derived from 15.87 to 84.12 percentiles of SB profiles among individual mocks. We would like to note that the simulations assume cosmological parameters of $H_0 = 67.11 \text{ km s}^{-1} \text{ Mpc}^{-1}$ and $\Omega_m = 0.3175$, which should not have a significant impact on the results below. We convert distances in the unit of arcsec for the simulated data to those in the unit of kpc at $z = 2.68$ with the Planck 2018 cosmological model (Planck Collaboration et al. 2020) as the galaxy sizes are matched and MUSE PSF are convolved in the unit of arcsec.

The left panel of Figure 7 shows a comparison of the observed and simulated mean-stacked SB profiles. The simulated UV continuum (gray dotted line) is well matched with the observations (black solid line), thanks to our manual 1.7 times expansion. The simulated Si II* λ 1533 profile (green dotted line) is more extended than the simulated UV continuum (gray dotted line) and consistent with the observed Si II* λ 1533 (blue solid line), though simulated Si II* halo is slightly less extended than observed within 1σ uncertainties.

The mean profiles can be biased toward bright halo sources, so we check whether the mean-stacked profiles are consistent

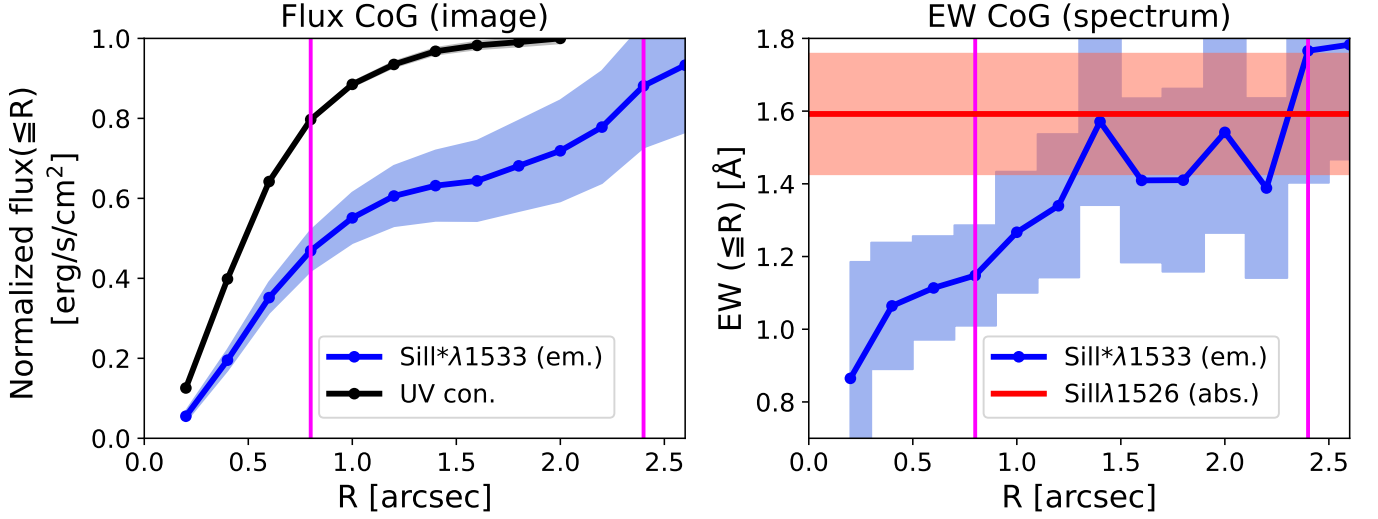


Fig. 5. Curve of growth (CoG) for Si II* flux and EW for MID= 1141. Left: Normalized fluxes within radius R as a function of R measured from the Si II* NB image (blue line) and the UV continuum BB image (black line). The blue shade indicates 1σ uncertainties for the Si II* flux. The vertical magenta lines show $R=0.8$ (galaxy scale) and $R=2.4$ (CGM scale), respectively. Right: EW(Si II*) CoG as a function of R shown by the blue line with the blue shade indicating 1σ uncertainties. EWs are measured in spectra extracted from the original minicube with growing apertures around the HST center. The red line and shade show the EW for Si II absorption at $R=0.8$ and its 1σ uncertainty, respectively.

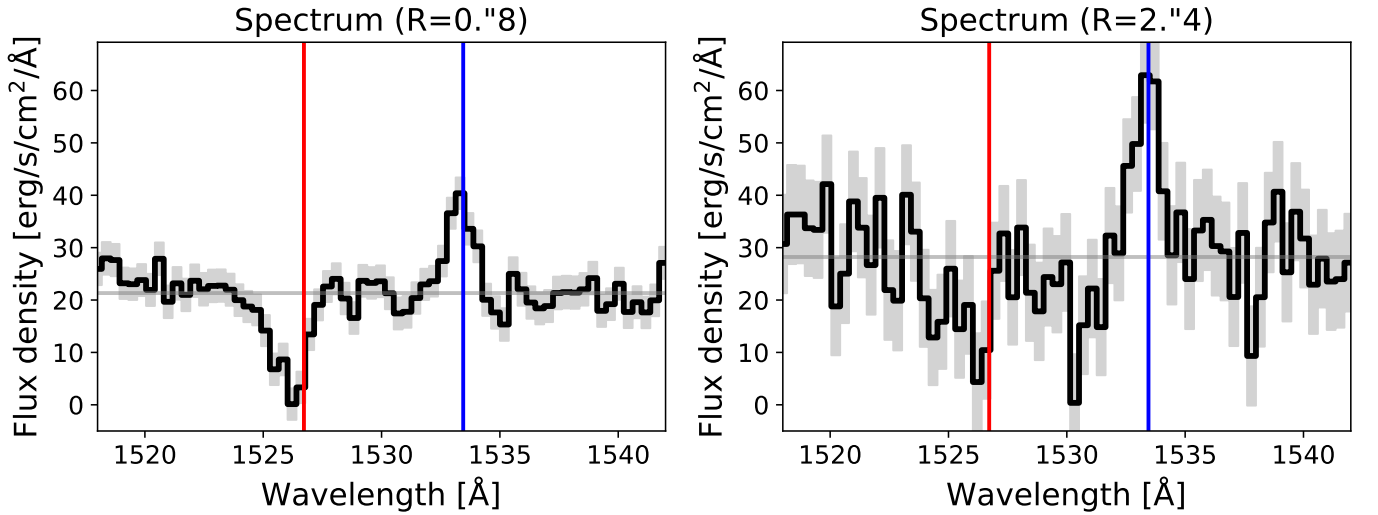


Fig. 6. Galaxy-scale and CGM-scale spectra for MID=1141. Left: The black line shows the spectrum extracted from the original minicube with a 0.8 aperture (radius) around the HST center. The gray solid line indicates the continuum. The gray shade shows 1σ uncertainties. The vertical red and blue lines indicate the rest-frame wavelength of Si II absorption and Si II* emission ($\text{EW}_{\text{abs}}(\text{Si II } \lambda 1526) = 1.6 \pm 0.2$ \AA and $\text{EW}_{\text{em}}(\text{Si II}^* \lambda 1533) = 1.1 \pm 0.1$ \AA). Right: The spectrum extracted from a 2.4 aperture around the HST center ($\text{EW}_{\text{em}}(\text{Si II}^* \lambda 1533) = 1.8 \pm 0.4$ \AA).

with the median-stacked profiles for the Si II* and the continuum (green and gray crosses, respectively) in the right panel of Figure 7. We confirm that they are consistent with each other, as for the MUSE observations of Si II*1533. The right panel also compares simulated mean-stacked SB profiles with PSF and LSF convolution versus without convolution, indicated by dotted and solid lines, respectively. The simulated galaxy indeed has significantly more extended Si II*1533 than the UV continuum in the intrinsic mock cubes, but the difference is mostly hidden by the MUSE PSF convolution⁵.

⁵ We check individual mocks and find that the shapes of the individual SB profiles (green dotted line) are fully dominated by the PSF.

We also check EW CoG of Si II*1533 emission and Si II1526 absorption lines for the simulations as shown in the left panel of Figure 8. The EWs of Si II*1533 emission and Si II1526 absorption are consistent at a CGM scale for both intrinsic cubes and PSF-convolved cubes, which are also seen on the mock spectra (see the middle and right panels of Figure 8). It means that the photon conservation works for the simulations with continuum pumping in the sense that the scattered photons are not more attenuated by dust than that stellar continuum. This is consistent with our observations for MID=1141.

From these comparisons, we conclude that our simulations with continuum pumping scenario can reproduce the observations. This lends extra support for the interpretation of Si II*

emission as a signature of continuum pumping. We note that the selection bias with the UV magnitude cut may have an impact on the observed result and this comparison. The mock observations are re-scaled by a factor of 1.7 to correct for the fact that the simulated galaxy is smaller than the observed ones (see above). The simulated galaxy is fainter than the observed one, though the range of absolute magnitudes overlaps (M_{UV} from -18 to -19). It would be interesting to test the selection bias with a larger and brighter simulated galaxy, or several, maybe at a slightly lower redshift.

4.3. Possible extension of the sample

We discuss possible strategies to extend the sample with existing data in this section. There are a few ways to increase the sample size: (1) sources at $z > 3.87$, which have other nebular line detections such as the $O\text{III}] \lambda\lambda 1661, 1666$ doublet and $He\text{II} \lambda 1640$ in the same catalog and the same field (with the same integration time), (2) sources located in shallower fields such as mosaic field (9×9-pointing with 10-hour integration, in the same catalog of Bacon et al. 2023) and MUSE-WIDE field (1-hour integration Herenz et al. 2017; Urrutia et al. 2019; Kerutt et al. 2022), (3) UV-bright sources at the same redshifts in other fields with similarly long integration times (> 30 hours) in MUSE archival data (e.g., Fossati et al. 2019; Lofthouse et al. 2020). The samples (1) and (2) are tested with the MUSE DR2 catalog (not including MUSE WIDE) in the same manner. We find that these less restrictive selection criteria do not help to increase the number of detections of Si II^* halos. Therefore, (3) using deep MUSE archival data for UV-bright galaxies with the same selection criteria would be the best way to extend the sample in the future.

In addition, (4) gravitationally lensed sources observed with MUSE (e.g., Richard et al. 2021; Claeysens et al. 2022, Claeysens et al. 2024 in prep.), would be useful to investigate more compact Si II^* halos in the future (see the right panel of Figure 7), which would be hidden by the PSF without the power of the magnification. We would like to note that they are not included in this pilot study as magnification can add complications and uncertainties. To investigate Si II^* halos at higher redshifts ($z \sim 3-6$), whose Si II^* lines are covered with MUSE, we could use (5) sources with systemic redshifts measured by nebular lines with James Webb Space Telescope (JWST), and (6) MUSE LAEs, whose systemic redshifts can be estimated by empirical relationships based on the $\text{Ly}\alpha$ line (Verhamme et al. 2018). We do not include these sources in this pilot study, considering uncertainties in wavelength calibration (e.g., Maseda et al. 2023; D'Eugenio et al. 2024; Meyer et al. 2024) and more severe cosmic dimming effects. It is future work for us to investigate higher- z sources.

5. Conclusions

To study the spatial distribution of the metal-enriched cool CGM at cosmic noon in emission, we search for extended Si II^* emission (fluorescent lines) using the MUSE HUDF data and catalog with 30-140 hour integration times. We construct a sample of 39 galaxies with systemic redshifts at $z = 2.07-3.87$, at which the $[\text{C III}] \lambda 1907, \text{C III}] \lambda 1909$ doublet nebular lines and at least one of the $\text{Si II}^* \lambda 1265, 1309, 1533$ lines are redshifted into the MUSE wavelength range. Our major results are summarized as follows.

1. Five individual $\text{Si II}^* \lambda 1533$ halos are confirmed to be present from statistical tests with surface brightness profiles. These are the first detections of extended Si II^* emission.

2. We stack images of $\text{Si II}^* \lambda 1533$ line for a subsample of 13 UV-bright galaxies. We confirm the presence of stacked $\text{Si II}^* \lambda 1533$ halos, which may imply that metal-enriched CGM is common for UV-bright galaxies. We also stack images of $\text{Si II}^* \lambda 1265, 1309, 1533$ for 14 UV-bright galaxies and detect a Si II^* halo. If we stack fainter galaxies or remove the five individually-detected halos from stacking, we get nondetections of Si II^* halos. We need a larger sample to draw a firm conclusion.
3. We find that the EW of the absorption line and fluorescent emission line are roughly equal when integrated out to large distances for $\text{MID}=1141$. This suggests that photons are conserved and that the emission line is mostly due to pumping from the stellar continuum.
4. We test the presence of Si II^* halos in zoom-in simulations, which account only for continuum pumping. After re-scaling the mock observations to correct for the fact that the simulated galaxy is smaller than the observed one, we find that the simulated halos are consistent with the observed stacked halo within 1σ uncertainties. This lends extra support for the interpretation of Si II^* emission as a signature of continuum pumping.
5. The best way to extend our sample with existing data in the future is using deep MUSE and KCWI archival data for UV-bright galaxies with the same selection criteria.

KCWI or BlueMUSE (Richard et al. 2019) will allow us to investigate HI $\text{Ly}\alpha$ halos for Si II^* halos detected with MUSE. BlueMUSE will also make it possible to individually detect Si II^* halos of more diverse sources and to study their statistical properties thanks to a more moderate cosmic dimming effect at $z \approx 2$ (by a factor of three, compared to $z \approx 3$). Such larger samples would be useful to improve the stacking experiments (see also Section 4.3) and to study spectral variations at different radii from the centers of galaxies as done for $\text{Ly}\alpha$ (Wisotzki et al. 2018; Guo et al. 2023c,b). Such studies will be advanced more with better sensitivities and higher spatial resolutions achieved by extremely large telescopes such as Thirty-meter telescope (TMT), one of whose key science cases is CGM mapping with WFOS (Skidmore et al. 2015), as well as European-Extremely large telescope (E-ELT).

Acknowledgements. HK acknowledges support from the Japan Society for the Promotion of Science (JSPS) Overseas Research Fellowship (202160056) as well as JSPS Research Fellowships for Young Scientists (202300224, 23KJ2148). HK thanks Yuri Nagai, an academic assistant at NAOJ, for her wonderful support. VM acknowledges support from the Nederlandse Organisatie voor Wetenschappelijk Onderzoek (NWO) grant 016.VIDI.189.162 ('ODIN'). AV and TG are supported by the SNF grant PP00P2 211023. T.N. acknowledges support from Australian Research Council Laureate Fellowship FL180100060. I.P. acknowledges funding by the European Research Council through ERC-AdG SPECMAP-CGM, GA 101020943. This work is based on observations taken by VLT, which is operated by European Southern Observatory. This research made use of Astropy⁶, which is a community-developed core Python package for Astronomy (The Astropy Collaboration et al. 2013, 2018), and other software and packages:MPDAF (Piqueras et al. 2019), PHOTUTILS, Numpy (Harris et al. 2020), Scipy (Virtanen et al. 2020), and matplotlib (Hunter 2007).

References

- Bacon, R., Accardo, M., Adjali, L., et al. 2010, Proceedings of the SPIE, 7735, 773508, conference Name: Ground-based and Airborne Instrumentation for Astronomy III Place: eprint: arXiv:2211.16795 ADS Bibcode: 2010SPIE.7735E..08B
- Bacon, R., Brinchmann, J., Conseil, S., et al. 2023, Astronomy & Astrophysics, 670, A4

⁶ <http://www.astropy.org>

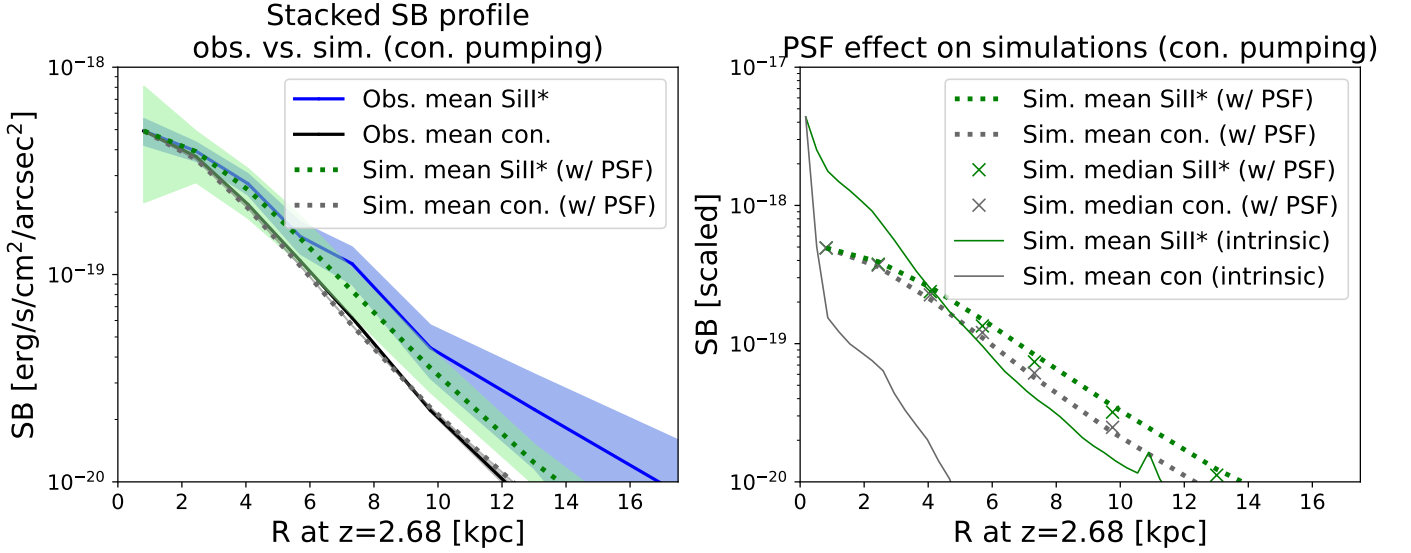


Fig. 7. Stacked SB profiles of our observations and of zoom-in simulations from Mauerhofer et al. (2021). Left: Comparison of stacked SB profiles. The blue and black solid lines show observed mean-stacked SB profiles of Si II*1533 and continuum, respectively. The blue shade indicates 1σ uncertainties for Si II*1533. The observed continuum is normalized at $R = 0$ to the peak of the observed Si II*1533. The green and gray dotted lines (shades) show mean-stacked SB profiles of Si II*1533 and continuum, respectively, for the simulations after PSF and LSF convolution (their 1σ uncertainties, which correspond to 15.87 to 84.13 percentile of SB profiles for individual mocks). They are normalized at $R = 0$ to the peak of the observed Si II* profile. Right: Stacked SB profiles for simulations. The green and gray dotted (solid) lines show the mean-stacked SB profiles of Si II*1533 and continuum, respectively, with (without) PSF and LSF convolution. The green and gray crosses show the median-stacked SB profiles of Si II*1533 and continuum, respectively, with PSF and LSF convolution. They are scaled by the same factor as used in the left panel.

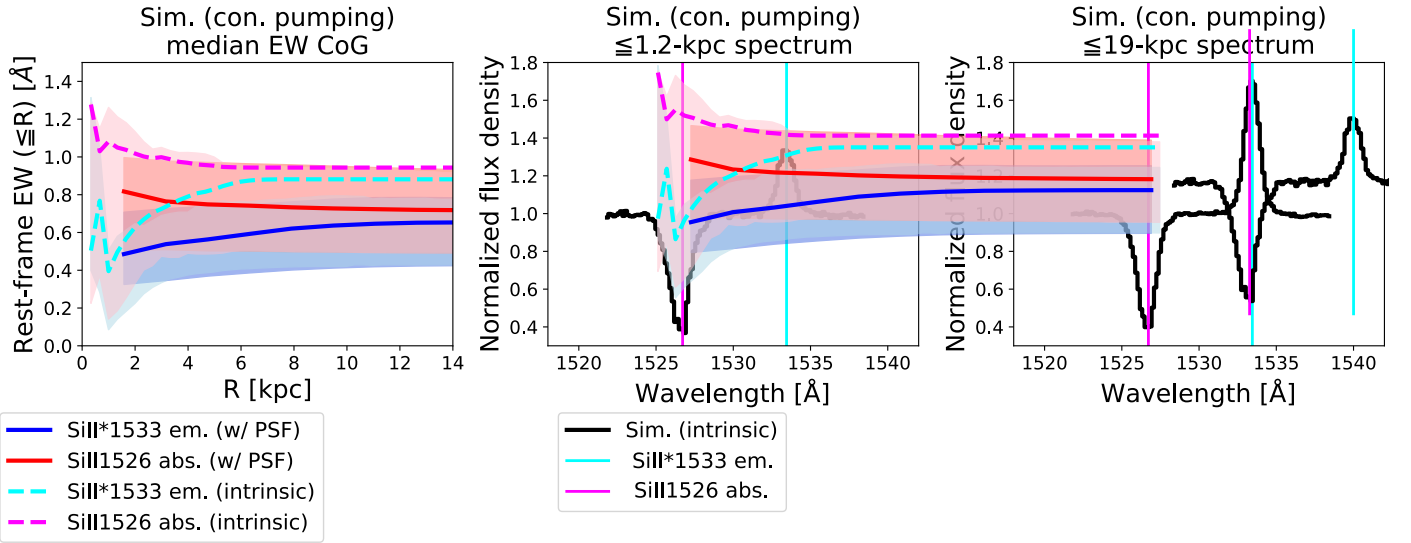


Fig. 8. EW CoG and spectra of the simulations with continuum pumping. Left: The median cumulative EW in rest-frame as a function of R . The blue and red solid lines (shades) indicate the EW of Si II*1533 emission and Si II*1526 absorption lines (their 1σ uncertainties) with MUSE PSF convolution, respectively. The cyan and magenta dashed lines (shades) show the intrinsic EW of Si II*1533 emission and Si II*1526 absorption lines (their 1σ uncertainties). Middle: The median spectrum extracted from the intrinsic mock cube with a 1.2 kpc aperture (galaxy scale) shown by the black line. The cyan and magenta lines show the wavelength of Si II*1533 emission and Si II*1526 absorption lines, respectively. Right: The median spectrum extracted from the intrinsic mock cube with a 19 kpc aperture (CGM scale).

Bacon, R., Conseil, S., Mary, D., et al. 2017, *Astronomy & Astrophysics*, 608, A1
 Berry, M., Gawiser, E., Guaita, L., et al. 2012, *The Astrophysical Journal*, 749, 4
 Blaizot, J., Garel, T., Verhamme, A., et al. 2023, *Monthly Notices of the Royal Astronomical Society*, 523, 3749, aDS Bibcode: 2023MNRAS.523.3749B
 Bordoloi, R., Simcoe, R. A., Matthee, J., et al. 2023, EIGER IV: The cool $10^{10} M_{\odot}$ circumgalactic environment of high- z galaxies reveals remarkably efficient IGM enrichment, arXiv:2307.01273 [astro-ph]
 Bradley, L., Sipőcz, B., Robitaille, T., et al. 2021, *astropy/photutils*: 1.3.0
 Burchett, J. N., Rubin, K. H. R., Prochaska, J. X., et al. 2021, *The Astrophysical Journal*, 909, 151

Carniani, S., Venturi, G., Parlanti, E., et al. 2023, JADES: The incidence rate and properties of galactic outflows in low-mass galaxies across $3 < z < 9$, publication Title: arXiv e-prints ADS Bibcode: 2023arXiv230611801C
 Carr, C., Scarlata, C., Panagia, N., & Henry, A. 2018, *The Astrophysical Journal*, 860, 143
 Chen, H.-W., Gauthier, J.-R., Sharon, K., et al. 2014, *Monthly Notices of the Royal Astronomical Society*, 438, 1435
 Chen, H.-W., Zahedy, F. S., Boettcher, E., et al. 2020, *Monthly Notices of the Royal Astronomical Society*, 497, 498, publisher: OUP ADS Bibcode: 2020MNRAS.497..498C

- Chen, Y., Steidel, C. C., Erb, D. K., et al. 2021, *Monthly Notices of the Royal Astronomical Society*, 508, 19
- Claeyssens, A., Richard, J., Blaizot, J., et al. 2022, *Astronomy & Astrophysics*, 666, A78
- Dessauges-Zavadsky, M., D’Odorico, S., Schaerer, D., et al. 2010, *Astronomy and Astrophysics*, 510, A26, aDS Bibcode: 2010A&A...510A..26D
- D’Eugenio, F., Cameron, A. J., Scholtz, J., et al. 2024, JADES Data Release 3 – NIRSpec/MSA spectroscopy for 4,000 galaxies in the GOODS fields, publication Title: arXiv e-prints ADS Bibcode: 2024arXiv240406531D
- Du, X., Shapley, A. E., Reddy, N. A., et al. 2018, *The Astrophysical Journal*, 860, 75
- Dutta, R., Fossati, M., Fumagalli, M., et al. 2023, *Monthly Notices of the Royal Astronomical Society*, 522, 535
- Dutta, S., Muzahid, S., Schaye, J., et al. 2024, *Monthly Notices of the Royal Astronomical Society*, 528, 3745, aDS Bibcode: 2024MNRAS.528.3745D
- Epinat, B., Contini, T., Finley, H., et al. 2018, *Astronomy & Astrophysics*, 609, A40
- Erb, D. K., Li, Z., Steidel, C. C., et al. 2023, *The Astrophysical Journal*, 953, 118, aDS Bibcode: 2023ApJ...953..118E
- Erb, D. K., Pettini, M., Shapley, A. E., et al. 2010, *The Astrophysical Journal*, 719, 1168
- Erb, D. K., Quider, A. M., Henry, A. L., & Martin, C. L. 2012, *The Astrophysical Journal*, 759, 26
- Feltre, A., Maseda, M. V., Bacon, R., et al. 2020, *Astronomy & Astrophysics*, 641, A118
- Ferland, G. J., Korista, K. T., Verner, D. A., et al. 1998, *Publications of the Astronomical Society of the Pacific*, 110, 761, publisher: The University of Chicago Press
- Finley, H., Bouché, N., Contini, T., et al. 2017, *Astronomy & Astrophysics*, 605, A118
- Fossati, M., Fumagalli, M., Lofthouse, E. K., et al. 2019, *Monthly Notices of the Royal Astronomical Society*, 490, 1451, publisher: OUP ADS Bibcode: 2019MNRAS.490.1451F
- France, K., Nell, N., Green, J. C., & Leitherer, C. 2010, *The Astrophysical Journal*, 722, L80
- Fujimoto, S., Ouchi, M., Ferrara, A., et al. 2019, *The Astrophysical Journal*, 887, 107
- Gazagnes, S., Mauerhofer, V., Berg, D. A., et al. 2023, *The Astrophysical Journal*, 952, 164, aDS Bibcode: 2023ApJ...952..164G
- Ginolfi, M., Jones, G. C., Béthermin, M., et al. 2020, *Astronomy & Astrophysics*, 633, A90
- Greene, J., Bezanson, R., Ouchi, M., Silverman, J., & Group, t. P. G. E. W. 2022, *The Prime Focus Spectrograph Galaxy Evolution Survey*, arXiv:2206.14908 [astro-ph]
- Guo, Y., Bacon, R., Bouché, N. F., et al. 2023a, *Nature*, 624, 53, arXiv:2312.05167 [astro-ph]
- Guo, Y., Bacon, R., Wisotzki, L., et al. 2023b, *Spatially-resolved Spectroscopic Analysis of Ly α Haloes: Radial Evolution of the Ly α Line Profile out to 60 kpc*, arXiv:2309.06311 [astro-ph]
- Guo, Y., Bacon, R., Wisotzki, L., et al. 2023c, *Median Surface Brightness Profiles of Lyman- α Haloes in the MUSE Extremely Deep Field*, arXiv:2309.05513 [astro-ph]
- Harris, C. R., Millman, K. J., Van Der Walt, S. J., et al. 2020, *Nature*, 585, 357
- Herenz, E. C., Urrutia, T., Wisotzki, L., et al. 2017, *Astronomy & Astrophysics*, 606, A12
- Hunter, J. D. 2007, *Computing in Science & Engineering*, 9, 90
- Illingworth, G. D., Magee, D., Oesch, P. A., et al. 2013, *The Astrophysical Journal Supplement Series*, 209, 6
- Inami, H., Bacon, R., Brinchmann, J., et al. 2017, *Astronomy & Astrophysics*, 608, A2
- Jaskot, A. E. & Oey, M. S. 2014, *The Astrophysical Journal*, 791, L19
- Johnson, S. D., Chen, H.-W., Straka, L. A., et al. 2018, *The Astrophysical Journal*, 869, L1
- Kerutt, J., Wisotzki, L., Verhamme, A., et al. 2022, *Astronomy & Astrophysics*, 659, A183
- Kramarenko, I. G., Kerutt, J., Verhamme, A., et al. 2023, *Monthly Notices of the Royal Astronomical Society*, 527, 9853, arXiv:2305.07044 [astro-ph]
- Kusakabe, H., Verhamme, A., Blaizot, J., et al. 2022, *Astronomy & Astrophysics*, 660, A44
- Leclercq, F., Bacon, R., Verhamme, A., et al. 2020, *Astronomy & Astrophysics*, 635, A82
- Leclercq, F., Bacon, R., Wisotzki, L., et al. 2017, *Astronomy & Astrophysics*, 608, A8
- Leclercq, F., Verhamme, A., Epinat, B., et al. 2022, *Astronomy & Astrophysics*, 663, A11, arXiv:2203.05614 [astro-ph]
- Lee, K.-G., Hennawi, J. F., Stark, C., et al. 2014, *The Astrophysical Journal*, 795, L12
- Lehner, N., O’Meara, J. M., Howk, J. C., Prochaska, J. X., & Fumagalli, M. 2016, *The Astrophysical Journal*, 833, 283
- Lofthouse, E. K., Fumagalli, M., Fossati, M., et al. 2020, *Monthly Notices of the Royal Astronomical Society*, 491, 2057, publisher: OUP ADS Bibcode: 2020MNRAS.491.2057L
- Lopez, S., Tejos, N., Ledoux, C., et al. 2018, *Nature*, 554, 493, aDS Bibcode: 2018Natur.554..493L
- Luo, B., Brandt, W. N., Xue, Y. Q., et al. 2017, *The Astrophysical Journal Supplement Series*, 228, 2, publisher: IOP ADS Bibcode: 2017ApJS...228....2L
- Martin, C. L., Shapley, A. E., Coil, A. L., et al. 2013, *The Astrophysical Journal*, 770, 41
- Maseda, M. V., Lewis, Z., Matthee, J., et al. 2023, *JWST/NIRSpec Measurements of Extremely Low Metallicities in High Equivalent Width Lyman- α Emitters*, arXiv:2304.08511 [astro-ph]
- Mauerhofer, V., Verhamme, A., Blaizot, J., et al. 2021, *Astronomy & Astrophysics*, 646, A80
- Meyer, R. A., Oesch, P. A., Giovinazzo, E., et al. 2024, *JWST FRESCO: a comprehensive census of H β +[OIII] emitters at 6.8*, publication Title: arXiv e-prints ADS Bibcode: 2024arXiv240505111M
- Moffat, A. F. J. 1969, *Astronomy and Astrophysics*, 3, 455, aDS Bibcode: 1969A&A.....3..455M
- Momose, R., Ouchi, M., Nakajima, K., et al. 2014, *Monthly Notices of the Royal Astronomical Society*, 442, 110
- Morrissey, P. 2018, *The Astrophysical Journal*
- Méndez-Hernández, H., Cassata, P., Ibar, E., et al. 2022, *Astronomy & Astrophysics*, 666, A56, arXiv:2206.08923 [astro-ph]
- Oke, J. B. & Gunn, J. E. 1983, *The Astrophysical Journal*, 266, 713, aDS Bibcode: 1983ApJ...266..713O
- Piqueras, L., Conseil, S., Shepherd, M., et al. 2019, *Astronomical Data Analysis Software and Systems XXVI ASP Conference Series*, 521, 545, conference Name: Astronomical Data Analysis Software and Systems XXVI ADS Bibcode: 2019ASPC..521..545P
- Planck Collaboration, Aghanim, N., Akrami, Y., et al. 2020, *Astronomy & Astrophysics*, 641, A6
- Prochaska, J. X., Kasen, D., & Rubin, K. 2011a, *The Astrophysical Journal*, 734, 24
- Prochaska, J. X., Weiner, B., Chen, H.-W., Mulchaey, J., & Cooksey, K. 2011b, *The Astrophysical Journal*, 740, 91
- Péroux, C. & Howk, J. C. 2020, *Annual Review of Astronomy and Astrophysics*, 58, 363
- Rafelski, M., Teplitz, H. I., Gardner, J. P., et al. 2015, *The Astronomical Journal*, 150, 31
- Rakic, O., Schaye, J., Steidel, C. C., & Rudie, G. C. 2012, *The Astrophysical Journal*
- Richard, J., Bacon, R., Blaizot, J., et al. 2019, *BlueMUSE: Project Overview and Science Cases*, arXiv:1906.01657 [astro-ph]
- Richard, J., Claeysens, A., Lagattuta, D., et al. 2021, *Astronomy & Astrophysics*, 646, A83
- Rubin, K. H. R., O’Meara, J. M., Cooksey, K. L., et al. 2018, *The Astrophysical Journal*, 859, 146
- Rubin, K. H. R., Prochaska, J. X., Ménard, B., et al. 2011, *The Astrophysical Journal*, 728, 55
- Schroetter, I., Bouché, N. F., Zabl, J., et al. 2021, *Monthly Notices of the Royal Astronomical Society*, 506, 1355
- Shaban, A., Bordoloi, R., Chisholm, J., et al. 2022, *The Astrophysical Journal*, 936, 77, aDS Bibcode: 2022ApJ...936...77S
- Shapley, A. E., Steidel, C. C., & Pettini, M. 2003, *The Astrophysical Journal*, 588
- Shull, J. M. & van Steenberg, M. 1982, *The Astrophysical Journal Supplement Series*, 48, 95, publisher: IOP ADS Bibcode: 1982ApJS...48..95S
- Skidmore, W., Dell’Antonio, I., Fukugawa, M., et al. 2015, *Thirty Meter Telescope Detailed Science Case: 2015*
- Steidel, C. C., Bogosavljević, M., Shapley, A. E., et al. 2011, *The Astrophysical Journal*, 736, 160
- Steidel, C. C., Bogosavljević, M., Shapley, A. E., et al. 2018, *The Astrophysical Journal*, 869, 123
- Steidel, C. C., Erb, D. K., Shapley, A. E., et al. 2010, *The Astrophysical Journal*, 717, 289
- Steidel, C. C., Strom, A. L., Pettini, M., et al. 2016, *The Astrophysical Journal*, 826, 159
- Sugahara, Y., Ouchi, M., Lin, L., et al. 2017, *The Astrophysical Journal*, 850, 51
- The Astropy Collaboration, Price-Whelan, A. M., Sipőcz, B. M., et al. 2018, *The Astronomical Journal*, 156, 123
- The Astropy Collaboration, Robitaille, T. P., Tollerud, E. J., et al. 2013, *Astronomy & Astrophysics*, 558, A33
- Tumlinson, J., Peebles, M. S., & Werk, J. K. 2017, *Annual Review of Astronomy and Astrophysics*, 55, 389, arXiv:1709.09180 [astro-ph]
- Turner, M. L., Schaye, J., Steidel, C. C., Rudie, G. C., & Strom, A. L. 2014, *Monthly Notices of the Royal Astronomical Society*, 445, 794
- Tytler, D., Gleed, M., Melis, C., et al. 2009

- Urbano Stawinski, S. M., Rubin, K. H. R., Prochaska, J. X., et al. 2023, *The Astrophysical Journal*, 951, 135
- Urrutia, T., Wisotzki, L., Kerutt, J., et al. 2019, *Astronomy & Astrophysics*, 624, A141
- Vasan G. C., K., Jones, T., Shajib, A. J., et al. 2024, *Spatially Resolved Galactic Winds at Cosmic Noon: Outflow Kinematics and Mass Loading in a Lensed Star-Forming Galaxy at $z=1.87$* , arXiv:2402.00942 [astro-ph]
- Verhamme, A., Garel, T., Ventou, E., et al. 2018, *Monthly Notices of the Royal Astronomical Society: Letters*, 478, L60
- Virtanen, P., Gommers, R., Oliphant, T. E., et al. 2020, *Nature Methods*, 17, 261
- Wang, B., Heckman, T. M., Zhu, G., & Norman, C. A. 2020, *The Astrophysical Journal*, 894, 149
- Werk, J. K., Prochaska, J. X., Cantalupo, S., et al. 2016, *The Astrophysical Journal*, 833, 54
- Wisotzki, L., Bacon, R., Blaizot, J., et al. 2016, *Astronomy & Astrophysics*, 587, A98
- Wisotzki, L., Bacon, R., Brinchmann, J., et al. 2018, *Nature*, 562, 229
- Wolfe, A. M., Turnshek, D. A., Smith, H. E., & Cohen, R. D. 1986, *The Astrophysical Journal Supplement Series*, 61, 249
- Xu, Y., Ouchi, M., Nakajima, K., et al. 2023, *Stellar and AGN Feedback Probed with Outflows in JWST Galaxies at $z=3-9$: Implications of Frequent Nearly-Spherical Galactic Fountains*, publication Title: arXiv e-prints ADS Bibcode: 2023arXiv231006614X
- Yuma, S., Ouchi, M., Drake, A. B., et al. 2017, *The Astrophysical Journal*, 841, 93
- Yuma, S., Ouchi, M., Drake, A. B., et al. 2013, *The Astrophysical Journal*, 779, 53
- Zabl, J., Bouché, N. F., Wisotzki, L., et al. 2021, *Monthly Notices of the Royal Astronomical Society*, 507, 4294, arXiv:2105.14090 [astro-ph]